Flow induced by acoustic streaming on surface-acoustic-wave devices and its application in biofouling removal: A computational study and comparisons to experiment

Subramanian K. R. S. Sankaranarayanan, Stefan Cular, Venkat R. Bhethanabotla,* and Babu Joseph
Sensors Research Laboratory, Department of Chemical and Biomedical Engineering, University of South Florida, Tampa, Florida 33620, USA

(Received 6 June 2007; revised manuscript received 28 April 2008; published 17 June 2008)

All transducers used in biological sensing suffer from fouling resulting from nonspecific binding of protein molecules to the device surface. The acoustic-streaming phenomenon, which results from the fluid motion induced by high-intensity sound waves, can be used to remove these nonspecifically bound proteins to allow more accurate determinations and reuse of these devices. We present a computational and experimental study of the acoustic-streaming phenomenon induced by surface acoustic waves.A coupled-field fluid-structure interaction (FSI) model of a surface-acoustic-wave (SAW) device based on a micrometer-sized piezoelectric substrate (YZ-$LiNbO_3$) in contact with a liquid loading was developed to study the surface-acoustic-wave interaction with fluid loading. The fluid domain was modeled using the Navier-Stokes equation; the arbitrary Lagrangian-Eulerian approach was employed to handle the mesh distortions arising from the motion of the solid substrate. The fluid-solid coupling was established by maintaining stress and displacement continuity at the fluid-structure interface. A transient analysis was carried out by applying a time-varying voltage to the transmitter interdigital transducer (IDT) fingers. Simulation results predict strong coupling of ultrasonic surface waves on the piezoelectric substrate with the thin liquid layer causing wave mode conversion from Rayleigh to leaky SAWs, which leads to acoustic streaming. The transient solutions generated from the FSI model were utilized to predict trends in acoustic-streaming velocity for varying design parameters such as voltage intensity, device frequency, fluid viscosity, and density. The induced streaming velocities typically vary from 1 μm/s to 1 cm/s, with the exact values dictated by the device operating conditions as well as fluid properties. Additionally, the model predictions were utilized to compute the various interaction forces involved and thereby identify the possible mechanisms for removal of nonspecifically bound proteins. Our study indicates that the SAW body force overcomes the adhesive forces of the fouling proteins to the device surface and the fluid-induced drag and lift forces prevent their reattachment. The streaming velocity fields computed using the finite-element model in conjunction with the proposed mechanism were used to identify the conditions leading to improved removal efficiency. Predictions of the model are in good agreement with those of simple analytical theories as well as the experimentally observed trends of nonspecific protein removal in typical SAW biosensing operations.

DOI: 10.1103/PhysRevE.77.066308 PACS number(s): 47.61.Fg, 47.85.−g, 47.11.−j, 47.85.Np

I. INTRODUCTION

Fluid motion induced from high-intensity sound waves is called acoustic streaming [1]. Surface acoustic waves propagating on the surface of a piezoelectric device can be used to induce acoustic streaming within the fluid [2–4]. The streaming phenomenon finds applications in various processes ranging from micromixing [5–7], surface reactions [8], and sonic cleaning [9] to biological detection [10] among several others [11–13].

SAWs and other transducer devices used in biological-species detection suffer from fouling that results from nonspecific binding of protein molecules [14–16] to the device surface. The acoustic-streaming phenomenon can be used to remove these nonspecifically bound proteins to allow more accurate determinations and reuse of these devices [17]. The generated sound fields cause tangential fluid motion along the interphase boundaries. These motions exert steady viscous stress on the boundary layer, leading to liquid circulation near the boundaries. Although these stresses are not large, they are still significant enough to remove loosely bound material on the surface of the device. Understanding the fluid dynamics in such a system is useful for efficient removal of nonspecifically bound proteins [18]. Toward this end, we focus on how acoustic streaming transforms into a velocity field profile near the interface region of the piezoelectric substrate and the fluid loading.

Surface acoustic waves are generated by the application of an alternating voltage signal to interdigital transducers patterned on a piezoelectric substrate [19–21]. The IDT geometry dictates the wavelength of the excited wave. The amplitudes of the SAWs depend on the applied voltage input, and are typically in the nanometer range. SAWs such as Rayleigh waves have a displacement component normal to the propagation direction. When in contact with a liquid, they tend to couple strongly with the liquid and leak ultrasonic power into the fluid in the form of acoustic waves called leaky SAWs. The leaky SAWs decay exponentially with distance from the source. The SAW interaction creates a net pressure gradient in the direction of sound propagation in the fluid which leads to an internal, acoustically induced, streaming phenomenon. Experimentally, the resulting flow profiles can be captured using various techniques. Flow visualization

*Corresponding author. venkat@eng.usf.edu

 ©2008 The American Physical Society

employing a dye solution and a fluorescence video microscope has been utilized by Kondoh and Shiokawa [2,11,22,23]. On the other hand, Guttenberg *et al.* used fluorescent correlation microscopy where movements of fluorescent particles are evaluated at the focal point of a confocal microscope using time autocorrelation of the intensity fluctuations [3]. A velocity map can be generated by successive measurements at different positions inside the fluidic device.

Computational techniques such as finite-element (FE) methods present an alternative to the experiments and can be used for more precise calculation of the flow field and velocity. Most of the previous theoretical investigations were based on methods such as that of Campbell and Jones, which involves obtaining numerical solutions to the complex characteristic equations for leaky wave velocity or perturbational techniques, which treats the leaky wave as a first-order perturbation on the nonleaky wave associated with surface-wave propagation, when the mechanical properties of the fluid are neglected. These techniques include many simplifying approximations [24–30] and are typically used to study acoustic streaming in simplified geometries. FE models developed so far have been mostly limited to solving for the fluid domain where the solid motion is superimposed as a boundary condition [6,26]. To capture the dynamics of fluid-solid interaction, the equations of motion for the fluid elements must be solved in conjunction with the acoustoelectric equations for the motion of the solid. FE models involving coupling of fluid and solid domains have been constructed using acoustic elements for modeling the fluid region. However, these models solve only the simplified Navier-Stokes equation for the pressure field in the fluid and ignore viscous dissipation [31]. Uniform mean density and mean pressures are assumed, with the pressure solution being the deviation from the mean pressure, not the absolute pressure. The application of these models is limited to the study of wave damping.

A coupled-field analysis is required to analyze the interactions between the solid motion and the induced fluid flow. In the present case, the problem of interest requires us to model fluid motion which can be accomplished using fluid elements which solves the generalized Navier-Stokes equation. To the best of our knowledge, no FE model involving coupled-field analysis of fluid–piezoelectric-solid devices has been presented in the literature so far. In the present work, FE models involving fluid-piezoelectric interaction are developed to study flow profiles in the interface region of a SAW biosensor device. The coupled-field models are utilized to investigate methods for increasing induced acoustic-streaming velocity while minimizing the effect of streaming-induced removal forces on the antibody-sensing layer in immuno-SAW sensors. Parameters studied in this model include voltage intensity, frequency, fluid density, and viscosity. The transient solutions generated from the model are used to predict trends in acoustic-streaming velocity. Comparisons of model predicted trends with experimental data on the removal of nonspecifically bound proteins from the sensing layers are also presented.

II. BIOFOULING OF SAW DEVICES

Biofouling of surfaces is one of the most common and significant problem in medical instruments, implantable materials, diagnostic systems, and sensors utilized for detection of biochemical species [32–34]. As a result, there has been a great deal of interest in devising strategies which can help minimize surface fouling. Most of the approaches that have been employed so far rely on modifying the surface chemistry or functionalization with polymeric groups such as poly(ethylene glycol) (PEG) to resist the nonspecific adsorption of proteins [35,36]. However, the auto-oxidation of the terminal hydroxyl group in PEG into aldehydes can damage the specific proteins employed for sensing applications [37]. Similarly, self-assembled monolayers of alkanethiolates on gold have also been found to be effective at minimizing the nonspecific adsorption of proteins and biomolecules [38]. However, this technique is not general and is not applicable for preventing protein adsorption on many common surfaces, including metal oxides, which are often employed as waveguides. Other commonly used approaches have involved grafting either phospholipids or derivatives of phosphorylcholine onto surfaces [39]. An alternative to chemical approaches is to employ acoustic energy to stress the bonds between the sensing film and analyte, forcing only the analyte with higher affinity (i.e., specific proteins) for the sensing film to stay bound. Recent experimental studies by Cular *et al.* have shown the applicability of Rayleigh wave modes to remove nonspecifically bound proteins from the surfaces of SAW devices [40]. The acoustic waves generated via piezoelectric coupling were found to effectively induce fluid motion (also termed acoustic streaming) and physically force loosely bound nonspecific protein species from their binding sites. This led to improved biosensor response. In the present study, we utilize fluid-solid interaction models to investigate conditions for increasing induced acoustic-streaming velocities and forces to eliminate biofouling while minimizing the effect of streaming-induced removal forces on the antibody-sensing layer in immuno-SAW sensors.

A. Experimental use of acoustic streaming to clean surfaces

The experimental results of the removal of nonspecifically bound proteins using acoustic streaming induced by a SAW device are described in this section. These experimental observations demonstrate the concept of streaming-induced removal of nonspecifically bound proteins. A 108 MHz *YZ*-$LiNbO_3$ SAW device was fabricated and its surface was coated with an antibody layer (anti–mouse-IgG) in a 40 μm array pattern. The pattern mask was removed and the nonantibody-coated regions were subsequently coated with bovine serum albumin (BSA) as a blocking agent. An Alexa-488 fluorescently labeled 20 μl sample of BSA in phosphate-buffered saline (PBS) *p*H 7.4 was applied to the entire (antibody regions and BSA-blocked regions) microarray surface and allowed to incubate undisturbed for 1 h. After incubation, excess Alexa-488-labeled BSA was removed with a thorough 5 ml of PBS rinsing. The prepared device was placed in a microfluidic probing fixture, connected to the necessary equipment, and placed on a fluorescent microscope for intensity measurements. Full details of the complete experimental study are presented elsewhere by Cular *et al.* [40].

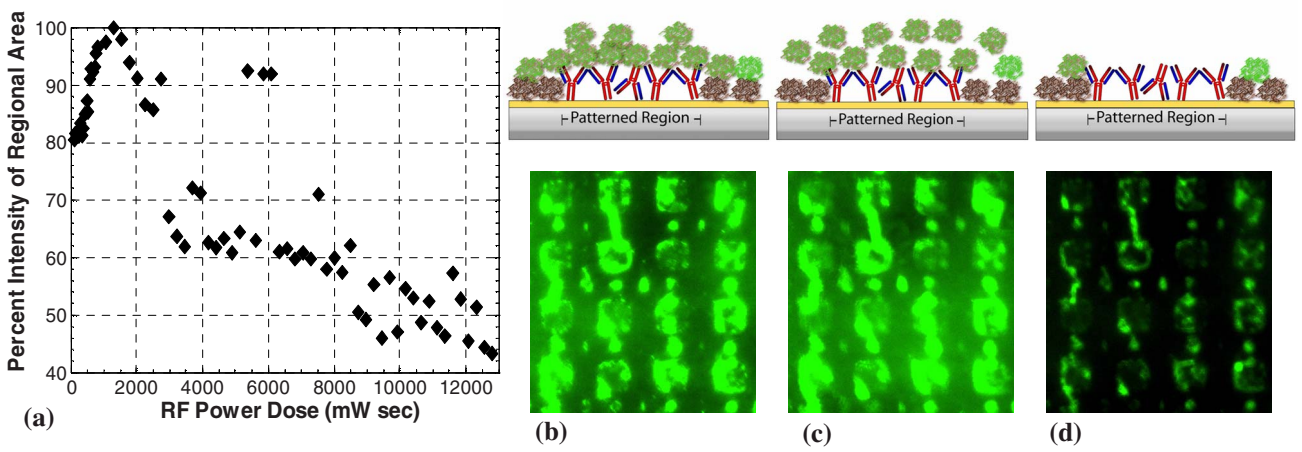

FIG. 1. (Color online) (a) Fluorescent intensity of Alexa-488-labeled BSA nonspecifically bound to the surface of a $LiNbO_3$ biosensor that was exposed to acoustic streaming. (b) Initial (rf power dose=0 mW s) fluorescent image (pseudocolored) of SAW device surface with illustration above. (c) First region (rf power dose=1600 mW s) fluorescent image (pseudocolored) of SAW device surface shortly after turning on the acoustic streaming with illustration above. (d) Nonspecifically bound BSA fluorescent image (pseudocolored) with illustration above of SAW device surface at end of experiment (rf power dose=12 500 mW s). The illustrations in (b), (c), and (d) depict the removal of nonspecifically bound proteins accomplished by the acoustic-streaming phenomenon induced by the Rayleigh wave interaction with the fluid medium.

The percent intensity of regional area of the microarray was recorded as a function of rf power dose, as shown in Fig. 1(a). During the acoustic streaming, a flow rate of 150 μl/min of 18 MΩ cm water was maintained except when acquiring images. Unwanted effects, such as photobleaching, have been corrected for through the use of a control experiment that exposed an identical SAW device to all of the same conditions minus the acoustic streaming. The sum total of these unwanted effects was less than 3% of the recorded signal.

The first region in the data starts shortly after the acoustic streaming begins and ends at 1600 mW s. The 20% increase in intensity is thought to be from an increase in the number of light-exposed fluorophores as shown by the greater distribution of Alexa-488 BSA in Fig. 1(c) from the initial conditions, Fig. 1(b). The second data region is a sharp decrease in intensity followed by a plateau (1600–8000 mW s). This region has the largest decrease of intensity, which correlates with the removal of the majority of loosely bound material. The third region in the graph is a transition region that removes the more strongly bound proteins. This is indicated from the scatter of the data in the dosage range of 8000 to 12 000 mW s. The data overall show a significant reduction of the nonspecifically bound BSA as shown by the reduction of intensity across the microarray in Fig. 1(d).

B. Motivation for the present study

The experimental study presented in the previous section illustrates the feasibility of the acoustic-streaming phenomenon to eliminate biofouling issues faced by SAW biosensors. These experimental observations demonstrate the concept of streaming-induced removal of nonspecifically bound proteins and confirm the findings that the SAW-induced acoustic-streaming phenomenon is an excellent method for surface stimulation in liquid environments. It should, however, be noted that too high a magnitude of streaming-induced forces can also lead to unbinding of specific proteins from the SAW device surface. Removal of specifically bound proteins, which are essential for detection purposes, would subsequently lead to reduction in the sensitivity, selectivity, and speed of response of SAW biosensors. It is therefore necessary to identify optimum conditions which can maximize the removal of nonspecifically bound proteins while having minimal removal effect on the antibody-sensing layer composed of specifically bound proteins.

In the present study, this is accomplished by developing a fluid-solid interaction finite-element model of acoustic-wave interaction with the fluid medium. The streaming velocity fields generated as a result of the acoustic-wave interaction with the fluid medium are investigated in detail. The effects of various parameters on the generated streaming velocity fields and streaming-induced forces are discussed. Parameters studied using this developed model include voltage intensity, SAW device frequency, fluid density, and viscosity. The transient solutions generated from the FSI model are used to predict trends in acoustic-streaming velocity and the possible mechanism of removal of nonspecifically bound proteins in SAW biosensors.

III. METHODS

The following sections discuss the continuum theory (Nyborg's streaming theory) and fluid-solid interaction finite-element-based approaches to compute the acoustic-streaming velocities and forces in SAW devices. The computational details involved in the two approaches are also discussed.

A. Acoustic-streaming theory

The governing equations for acoustic streaming were derived by Nyborg [1] and are given by

TABLE I. Leaky SAW velocity and streaming force calculated using Nyborg streaming equations with parameters derived from the Campbell-Jones method. SAW streaming force is calculated at $x=z=0$ for a 100 MHz device frequency and applied input voltage of 1 V.

Crystal orientation	Rayleigh wave velocity (m/s)	Water-loaded leaky SAW velocity	Leaky SAW wave number	Attenuation coefficient	SAW streaming force(N/m^2)
128° *YX*-$LiNbO_3$	3994	$3931+j68.1$	2768	2.47	3.22×10^7
YZ-$LiNbO_3$	3487	$3194+j268.3$	16409	1.92	4.05×10^8

$$\mu\nabla^2 v_2 - \nabla p_2 = F, \tag{3.1}$$

$$F = \rho_0\langle v_1 \cdot \nabla v_1 + v_1 \nabla \cdot v_1\rangle. \tag{3.2}$$

In the above equations, μ is the shear viscosity, ρ_0 is the constant equilibrium density, v_1 is the oscillatory particle velocity, v_2 is the acoustic-streaming velocity, p_2 is the steady state "dc" pressure, F is the nonlinear driving force term, and the angular brackets denote the time average over a sufficiently large number of cycles [41,42].

The leaky SAW propagates along the boundary and excites longitudinal waves into the liquid. The propagation constant (k_L) for leaky SAWs is a complex number, with the imaginary part accounting for the extent of energy dissipation into the fluid medium. The particle displacements in the normal (u_x) and tangential (u_z) directions in the liquid can be put in the following form:

$$u_x = A\exp(j\omega t)\exp(-jk_L x)\exp(-\alpha k_L z), \tag{3.3}$$

$$u_z = -jA\alpha\exp(j\omega t)\exp(-jk_L x)\exp(-\alpha k_L z),$$
$$\text{where}\quad \alpha = 1-(v_L/v_w)^2. \tag{3.4}$$

A refers to the amplitude of SAW displacement; $\omega=2\pi f$ is the angular frequency; v_L and v_w represent the leaky and longitudinal wave velocities, respectively. The wave number (k_L) and velocity (v_L) of the leaky SAW can be computed by extending the method of Campbell and Jones to solid-liquid structures assuming displacement and stress continuity at the interface [24,25].

The oscillatory particle velocity v_1 can be found using $v=\partial u/\partial t$. The first-order velocity is comprised of two terms. The first varies with z as $\exp(-\alpha z)$ and represents the mass loading response of the fluid [4,43,44]. The second term (ignored in the solution) varies with z as $\exp[-(1+j)\beta z]$, where $\beta=\omega/\sqrt{2}\nu$, and represents the viscous response of the fluid. For the case of water loading at typical operational frequency of 100 MHz, $1/\beta$, which represents the viscous boundary layer, was found to be less than 0.02 μm. Hence $\beta z \gg 1$ and the second term can be ignored. Substituting the first-order velocity into Eq. (3.2), we obtain the following components of the force **F**:

$$F_x = -\rho_0(1+\alpha_1^2)A^2\omega^2 k_i \exp 2(k_i x + \alpha_1 k_i z), \tag{3.5}$$

$$F_z = -\rho_0(1+\alpha_1^2)A^2\omega^2 \alpha_1 k_i \exp 2(k_i x + \alpha_1 k_i z), \tag{3.6}$$

where $\alpha=j\alpha_1$ and $k_L=k_r+jk_i$. The force calculated above acts as a body force near the SAW-fluid interface. The decaying exponential factors in v_1 limit the extent of the force in the fluid. This force, which varies as the square of the first-order velocity, in turn produces the second-order velocity v_2. Substitution of the above equations (3.5) and (3.6) into (3.1) would allow for predicting the acoustic-streaming velocity induced as a result of SAW streaming. The leaky SAW velocities, wave numbers, attenuation factors as well as the SAW streaming force calculated based on the above formulation for two different crystal orientations are summarized in Table I.

The first-order streaming velocity can be used to calculate the second-order streaming velocity. Longuet-Higgins has given the general expression for calculating the limiting value of the second-order streaming velocity (v_2) from the solution of the first-order velocity [45],

$$U = \frac{-jv_m}{4\omega}\frac{\partial v_m^*}{\partial x}(8\{1-\exp[-(1+j)\beta z]\} + 3(1+j)[\exp(-2\beta z)-1]). \tag{3.7}$$

In the above equation, only the real part is of physical significance. U represents the tangential streaming velocity just outside the viscous boundary layer. v_m is equal to $v_{1x}-v_0$, where v_{1x} is the x-directed first-order velocity and v_0 is the x-directed boundary condition on the first-order velocity field at the SAW interface. For $\beta z \gg 1$, the amplitude of the second-order velocity obtained by substituting Eq. (3.4) into Eq. (3.7) is given by

$$U \approx \frac{5}{4}\alpha A^2\omega k_i. \tag{3.8}$$

The streaming velocity calculated above depends primarily on the wave amplitude and the excitation frequency. The viscous effects have been neglected and the density effects are implicitly accounted for through the leaky wave number k_i.

B. Finite-element model

The sequential coupling algorithm in ANSYS [46] was utilized to simulate the fluid-structure interactions. In this iterative coupling procedure, each domain (solid piezoelectric and fluid) is solved sequentially and the governing matrix equations for the two are solved separately. The solver iterates between each physics field (piezoelectric and fluid) until loads transferred across the interfaces converge. The nonlinear transient fluid-solid interaction analysis involves the following set of equations.

1. Solid domain

The propagation of acoustic waves in piezoelectric materials is governed by the mechanical equations of motion and Maxwell's equations for electrical behavior [19,47]. The constitutive equations of piezoelectric media in linear range coupling the two are given by

$$T_{ij} = c^E_{ijkl} S_{kl} - e^t_{kij} E_k, \tag{3.9}$$

$$D_i = e_{ikl} S_{kl} + \varepsilon^S_{ik} E_k. \tag{3.10}$$

In the above equations, T_{ij} represent the components of stress, c^E_{ijkl} the elastic constant for constant electric field, S_{kl} the strain, E_k the electric field intensity, D_i the electric displacement, e^t_{kij} the piezoelectric constant, and ε^S_{ik} the permittivity for constant strain. The acoustic-wave propagation velocity is five orders of magnitude smaller than that of electromagnetic waves. Therefore, the quasistatic assumptions help reduce Maxwell's equations to $\partial D_i / \partial x_i = 0$ and $E_i = -\partial \phi / \partial x_i$, where φ represents the electric potential.

The components of strain are defined by

$$S_{ij} = \frac{1}{2}\left(\frac{\partial u_i}{\partial x_j} + \frac{\partial u_j}{\partial x_i}\right). \tag{3.11}$$

The equation of motion in the absence of internal body forces is given as

$$\frac{\partial T_{ij}}{\partial x_j} - \rho \frac{\partial^2 u_i}{\partial t^2} = 0, \tag{3.12}$$

where ρ is the density and u_i represent the components of displacement. Substituting and rearranging the above set of equations leads to a system of four coupled wave equations for the electric potential and the three component of displacement in piezoelectric materials, which are solved for the piezoelectric substrate or the solid domain:

$$-\rho \frac{\partial^2 u_i}{\partial t^2} + c^E_{ijkl} \frac{\partial^2 u_k}{\partial x_j \partial x_l} + e_{kij} \frac{\partial^2 \phi}{\partial x_k \partial x_j} = 0, \tag{3.13}$$

$$e_{ikl} \frac{\partial^2 u_k}{\partial x_i \partial x_l} - \varepsilon^S_{ik} \frac{\partial^2 \phi}{\partial x_i \partial x_j} = 0. \tag{3.14}$$

These coupled wave equations can be discretized and solved for generating displacement profiles and voltages at each element or node. The piezoelectric material displacements obtained from the above equations are applied to the fluid domain at each time step.

2. Fluid domain

The fluid is modeled as an incompressible, viscous, Newtonian fluid using the Navier-Stokes and continuity equations in the Eulerian frame of reference given below:

$$\rho\left(\frac{\partial v_f}{\partial t}\right) + v_f \cdot \nabla v_f + \nabla P - 2\eta \nabla \cdot D = 0, \tag{3.15}$$

$$\nabla \cdot v_f = 0. \tag{3.16}$$

Here, v_f, P, ρ, and η denote the fluid velocity, pressure, density, and viscosity, respectively. D is the rate of deformation tensor given by

$$D = \frac{1}{2}[\nabla v_f + (\nabla v_f)^t]. \tag{3.17}$$

3. Fluid-solid interaction

Discretization of the fluid and solid regions in the finite-element domain requires the use of either the Lagrangian or Eulerian frame of reference. The equation of motion for the structural phase (piezoelectric substrate) is described in the Lagrangian frame. The fluid domain can be described by either the Lagrangian or the Eulerian frame of reference. In the former, the mesh embedded in the fluid domain moves with the velocity of the fluid, while in the latter, the mesh, through which the fluid moves, is fixed. A purely Lagrangian frame is incapable of dealing with strong distortions of the fluid mesh. A purely Eulerian frame for the fluid domain introduces complexity in fluid-solid coupling. Therefore, mixed Lagrangian-Eulerian or arbitrary Lagrangian-Eulerian (ALE) methods are used for kinematical description of the fluid domain. The theory for the ALE method has been developed by Hughes *et al.* for viscous, incompressible flows [48]. In this method, the Lagrangian description is used for "almost contained" flows and the Eulerian description is used for regions where the mesh would be highly distorted if required to follow fluid motion. In the ALE framework, the fluid equation of motion can be written as [49]

$$\rho\left(\frac{\partial v_f}{\partial t}\right) + (v_f - w) \cdot \nabla v_f + \nabla P - 2\eta \nabla \cdot D = 0, \tag{3.18}$$

where w is the grid velocity such that $w \neq v_f \neq 0$.

To account for the fluid-solid interaction, an interface is defined across which displacements are transferred from solid to fluid and pressure from fluid to solid. The fluid mesh is continuously updated as the piezoelectric substrate undergoes deformation. The coupling conditions for the interface between the fluid and the solid region are the kinematics and equilibrium condition. The kinematic equation is the no-slip condition, i.e., the continuity of velocity,

$$v_f = v_s = \frac{\partial u}{\partial t}, \tag{3.19}$$

and the equilibrium condition is the interface continuity in traction replaced by continuity of stresses,

$$\sigma^S_{ij} n^S_j + \sigma^f_{ij} n^f_j = 0, \tag{3.20}$$

where n^S_j is the outward normal to the solid at the solid-liquid interface in the deformed configuration, so that $n^S_j = -n^f_j$ [the indices i and j define directions of components according to axes of the applied two-dimensional (2D) coordinate system]. The above equations are represented in terms of partial differential equations which are discretized using the finite-element technique [50,51].

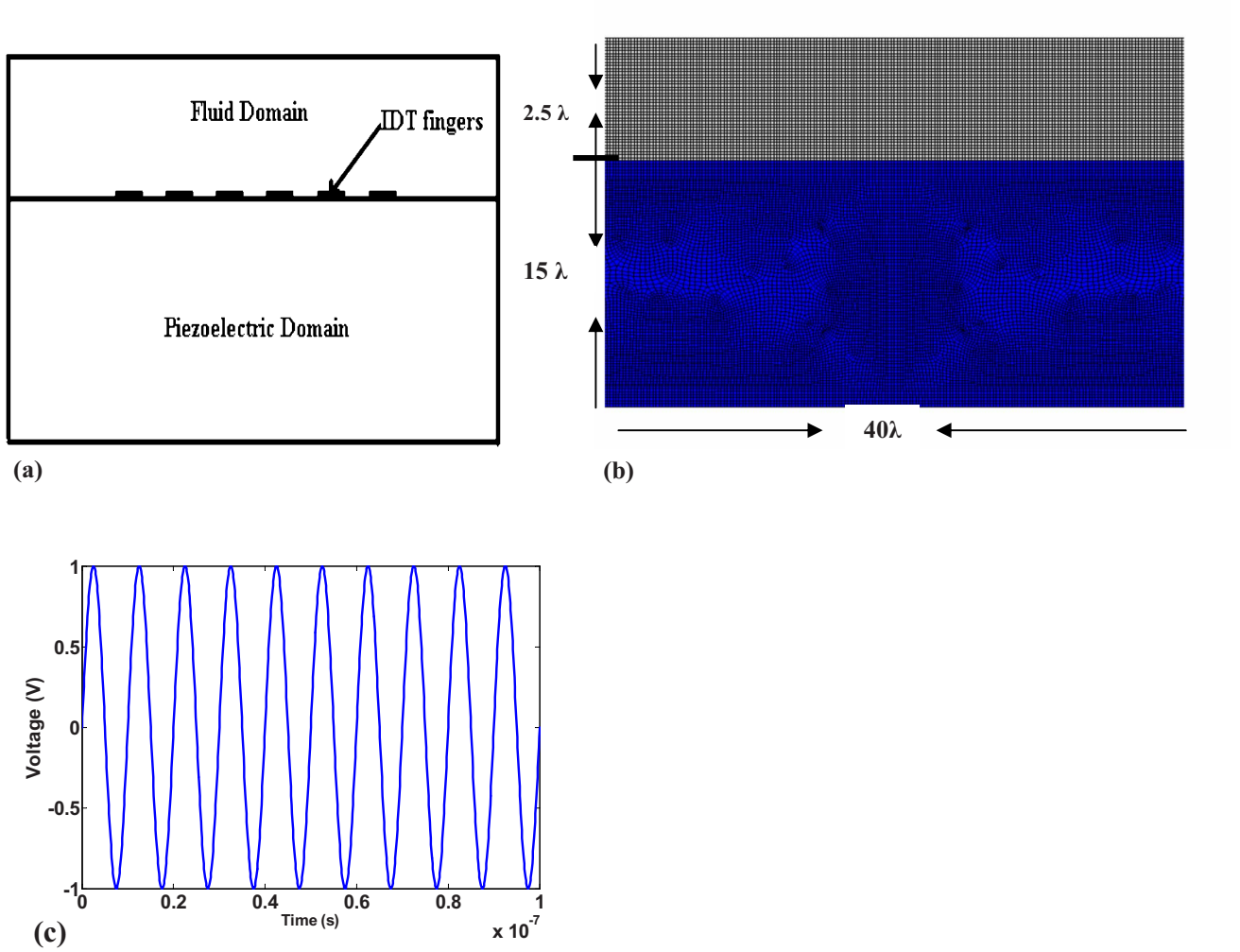

FIG. 2. (Color online) (a) Schematic of the simulated SAW device. Device is not drawn to scale. The IDT fingers are located at the center of the device on the fluid-piezoelectric interface. (b) Finite-element model of liquid loading on a SAW device. The meshed fluid domain is shown in green and the meshed solid piezoelectric domain is shown in purple. (c) Applied input voltage profile for excitation of the 100 MHz SAW device.

C. Computational details

A fluid-solid interaction model of the acoustic-streaming phenomenon using the finite-element technique is presented in this work. Rayleigh wave propagation on a SAW device represents a plane wave problem [23]. Hence, 2D FE models of a SAW device based on *YZ*-$LiNbO_3$ with a liquid loading were developed.

1. Solid domain

A micrometer-sized piezoelectric substrate with dimensions 800 μm propagation length$\times$500 μm depth was simulated to gain insights into the acoustic streaming in SAW devices. Three IDT finger pairs for the input port were defined at the surface of the *Y*-cut, *Z*-propagating $LiNbO_3$ substrate. The fingers were defined with periodicity of 34.87 μm. Eight-node quadrilateral coupled-field solid elements were used to model the solid piezoelectric domain. The IDT fingers were modeled as massless conductors and represented by a set of nodes coupled by voltage degrees of freedom (DOFs). A total of approximately 80 000 elements (more than 100 000 nodes) were generated. The model was created to ensure higher node density at the surface and throughout the middle of the device to study the different modes of surface acoustic waves, and the use of eight-node coupled-field (solid) elements with three DOFs ensured the same. Two DOFs provided the displacements in the longitudinal (x), and the normal (y) directions and the third was for the voltage.

2. Fluid domain

Four-node quadrilateral fluid elements were used to model the transient system involving the fluid region. The fluid properties of water were used in the simulations. The velocities are obtained from the conservation of momentum principle, and the pressure is obtained from the mass conservation principle. The fluid region with dimensions 800 μm length$\times$100 μm height was modeled as an infinite reservoir by applying pressure $P=0$ on the upper fluid

surface in Fig. 2. The standard k-ε model is used to study flow in the turbulent regime.

3. Structure excitation

The center frequency of SAW devices simulated in this work is in the range of megahertz. Hence, the structure was simulated for a total of 100 ns, with a time step of 0.5 ns. The excitation of the piezoelectric solid was provided by applying an ac voltage (with varying peak values and frequency of 100 MHz) on the transmitter IDT fingers as shown in Fig. 2(c).

D. Time averaging for steady-state streaming velocities

The finite-element model of SAW streaming presented here is utilized for determining steady-state streaming velocity profiles associated with a given transducer geometry and input acoustic pulse. The velocity v calculated from Eqs. (3.15) and (3.16) contains harmonically varying terms and a dc term. The latter induces acoustic streaming. When averaged over a longer time, the effect of the harmonically varying terms disappears and only the contributions from the dc part appear in the solution. The acoustic-streaming velocity ($\bar{v}_{a,i}$, $i=x$, y, and z) is therefore obtained by averaging v over a time period as follows:

$$\bar{v}_{a,i} = \frac{1}{T}\int_0^T v_i dt, \quad i = x, \ y, \ \text{and} \ z \tag{3.21}$$

where T is the time period of the wave propagation. The time averaging was applied during the various vibration cycles (e.g., the fifth cycle was comprised of simulation steps 81 and 100 and gives the streaming velocity values for $t=40-50$ ns). The streaming velocities calculated based on the time averaging during the 100th–120th cycles ($t=50-60$ ns) and at higher intervals do not differ significantly from the values computed at $t=40-50$ ns. Hence, the average streaming velocities were assumed to be cycle independent by this time ($t=40$ ns).

IV. RESULTS

The following sections discuss the wave mode conversions that result from the imposed fluid loading as well as the flow profiles of the induced fluid motion. The effects of various design parameters on the streaming velocity profiles are also presented.

A. Rayleigh wave mode conversion

When the surface-acoustic-wave propagation surface comes in contact with a liquid medium, mode conversion from Rayleigh to leaky SAWs occurs. These leaky SAWs propagate along the boundary and excite longitudinal waves into the fluid at Rayleigh angle (θ) given by [28,29]

$$\theta = \sin^{-1}\left(\frac{v_w}{v_R}\right), \tag{4.1}$$

where v_w and v_R are the wave velocities in the liquid and piezoelectric medium. This ultrasonic radiation mechanism is shown in Fig. 3.

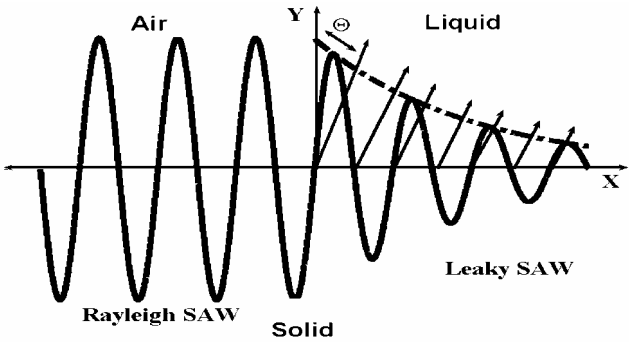

FIG. 3. Ultrasonic radiation into the fluid medium. The interaction of the Rayleigh wave with the fluid medium results in a wave mode conversion into leaky SAWs. These leaky SAWs propagate along the boundary between the piezoelectric and the fluid loading and excites longitudinal waves into the fluid at a Rayleigh angle θ.

The longitudinal sound waves generated in the fluid medium are attenuated by the viscous fluid during their transmission through the medium. The displacement profile along the fluid film thickness (i.e., the height of the liquid loading) for an applied voltage of 0.1 V is shown in Fig. 4. It can be seen that the mode conversion from Rayleigh to leaky SAWs leads to an exponential decay in the fluid. The extent of the decay is dictated by the applied input voltage as well as the viscous dissipation encountered by the longitudinal wave in the fluid medium. The leaky surface wave also decays along the propagation length as shown by the displacement contours in Fig. 5.

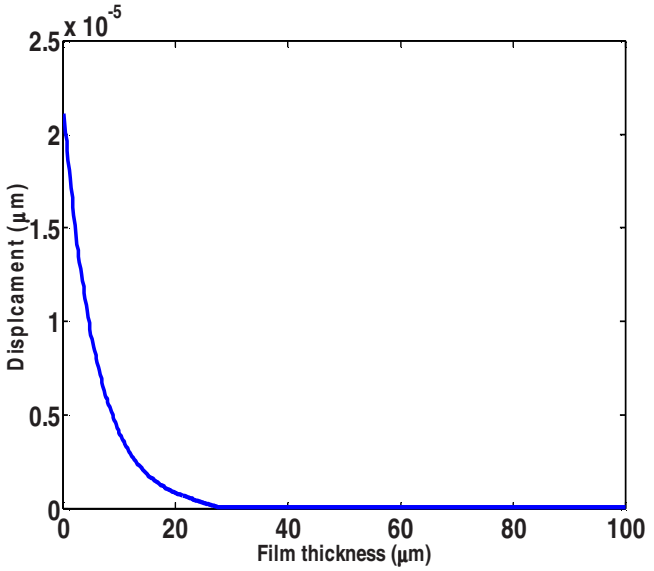

FIG. 4. (Color online) Displacement profile along the fluid film thickness induced as a result of leakage of ultrasonic SAW power into the fluid. The simulated exponential decay with distance from the source is similar to that of the leaky SAW. The displacement profiles depicted are for an applied input voltage of 0.1 V for a SAW device operating at 100 MHz. A voltage value of 0.1 V is chosen for the purpose of illustration. Qualitatively similar behavior is observed at other applied voltages.

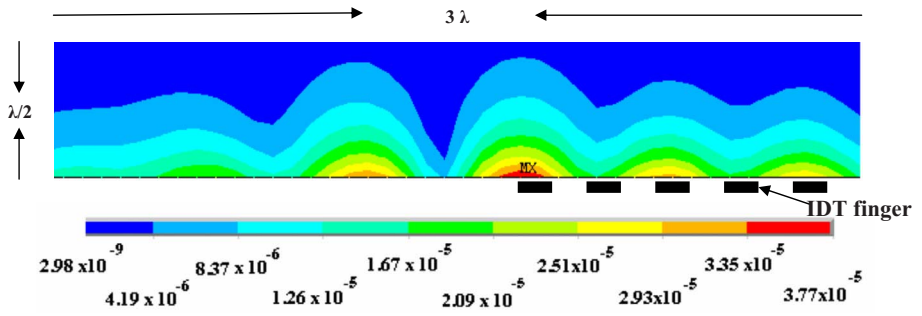

FIG. 5. (Color online) Contours showing particle displacement profile (μm) in the fluid region for an applied ac peak input voltage of 1 V in a SAW device operating at 100 MHz. The wave decays with distance from the IDT fingers located at the center of the SAW device. The location of the IDTs is shown for visualization purposes. The displacements in the solid have been suppressed for clarity. A voltage value of 1 V is chosen for the purpose of illustration. Qualitatively similar behavior is observed at other applied voltages.

B. Structural motion

The application of ac voltage on the IDT fingers located at the surface of the piezoelectric substrate results in mechanical deformations which cause acoustic wave propagation through the solid medium. The displacement wave forms through the depth of the piezoelectric substrate at two different locations along the SAW delay path are shown in Fig. 6. As can be seen from the depth profiles, most of the acoustic energy is confined to within a depth of 1–1.5 wavelengths into the substrate. As the acoustic wave propagates along the delay path, dissipation of acoustic energy occurs due to Rayleigh mode conversion into leaky SAWs. As a result, the solid displacement is dampened with distance along the delay path. The displacement amplitude of surface particles located at 10 μm distance from the IDTs is approximately 30 Å and reduces to 5 Å at 60 μm along the delay path for an applied input voltage of 1 V for a SAW device operating at 100 MHz.

C. Fluid motion

As brought out in the earlier sections, the mode conversion from Rayleigh to leaky SAWs results in longitudinal wave propagation into the fluid medium. If the intensity of the longitudinal waves propagating through the fluid is high enough, then the attenuation results in a net pressure gradient along the propagation direction of the wave. The induced gradient causes a flow in the fluid. This conversion of an attenuated sound wave into a steady flow represents a nonlinear effect termed acoustic streaming. The streaming effect that results from mode conversion is much stronger than that induced from a spatially constant amplitude plane wave [2].

The fluid motion induced by the IDTs at a time instant (i.e., $t=10$ ns) is shown in Fig. 7. The fluid is expelled by the transducers to the top and flows back to the IDT regions from the bottom and top. Depending on the extent of the viscous damping, the flow velocity decays rapidly with distance from the IDT.

It can be seen that the induced velocities are typically in μm/s. The maximum velocity occurs at the layer closest to the piezoelectric surface. The recirculation patterns resulting from the wave motion gives rise to eddy formation. With increasing time, these eddies rise through the fluid and break into smaller ones, thereby dissipating their energy while new ones are created at the interface. Thus, the generated sound fields cause tangential motion along the interphase boundaries. These motions exert steady viscous stress on boundaries where the circulation occurs, as shown in Fig. 7. Although these stresses are not large, they are still significant enough to remove loosely bound material on the surface of the device. Our simulation results indicate that the extent of recirculation decreases with increasing distance from the IDTs. It can therefore be seen from Fig. 8 that the generated shear stresses at the device surface also decay rapidly with distance from the IDT fingers. The optimization of design parameters such as fluid density, viscosity, and applied voltage amplitude and frequency which could help generate sufficient shear stresses along the entire delay path (typically

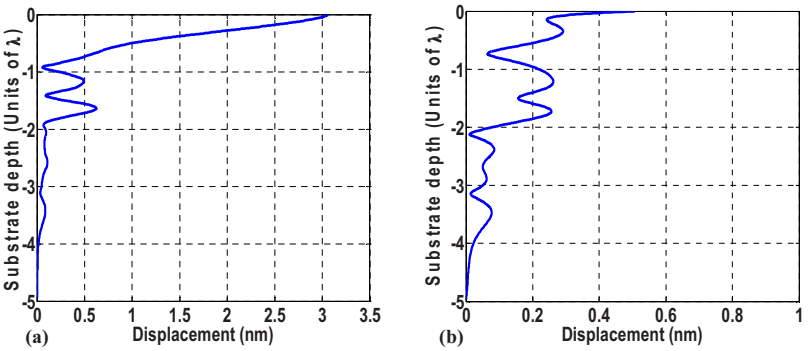

FIG. 6. (Color online) Normalized displacement profiles along the depth of the piezoelectric substrate. (a) and (b) represent the displacement profiles at two different locations (10 and 60 μm, respectively) along the SAW delay path.

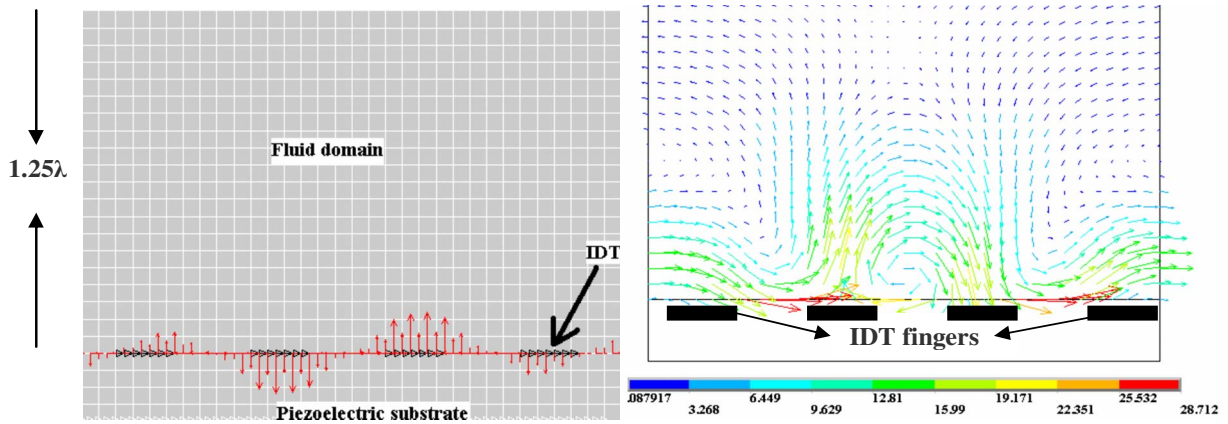

FIG. 7. (Color online) (a) Displacement of IDT fingers as indicated by arrows. (b) Velocity vector plot at a given time instant (t = 10 ns) showing fluid recirculation over the IDT region shown in (a). The observed velocities are in μm/s. The location of the IDTs is shown for visualization purposes. The motion of the IDT fingers results in the observed fluid recirculation patterns. The fluid is pumped perpendicularly to the IDT fingers and is sucked in parallel to them.

100λ) thereby facilitating removal of nonspecifically bound proteins. The subsequent sections discuss the effect of some of the above mentioned parameters on the induced streaming velocity.

A series of simulations were performed to observe the effect of changing voltage intensity, excitation frequency, and fluid properties such as viscosity and density on the streaming velocity and its patterns. It is observed that the flow patterns described above are not influenced by the simulation conditions, but the magnitude of the acoustic-streaming velocity is strongly influenced. Therefore, for the following analyses, only the variations of the streaming velocity magnitude along vortex centers located at various positions along the delay path are compared and discussed in the subsequent sections.

D. Streaming velocity

The computational details involving calculation of the time-averaged streaming velocity using the fluid-solid interaction models has been discussed in Sec. III. The maximum streaming velocity value is found to be approximately 0.220 mm/s while the maximum instantaneous velocities reach 20 mm/s in the regions close to the IDTs for applied voltages up to 1 V and excitation frequencies up to 100 MHz. Experimentally, the observed streaming velocities are also much smaller than 20 mm/s for the loading conditions simulated in the present work and hence, for a fluid film thickness of 100 μm, the flow is characterized by Reynolds numbers smaller than 1. Hence the flow is completely laminar. For these flow conditions, the effect of input parameters such as applied voltage intensity and SAW device operational frequency as well as fluid properties such as viscosity and density on the time-averaged streaming velocity profiles is discussed in detail in the following sections.

1. Effect of voltage intensity

The effect of varying input voltage intensity on the time-averaged streaming velocities is shown in Fig. 9. The components of acoustic-streaming velocities tangential and normal to the SAW device substrate along a fictitious vertical line passing through the device center are shown in Fig. 9. The fluid velocities are thus obtained at different positions

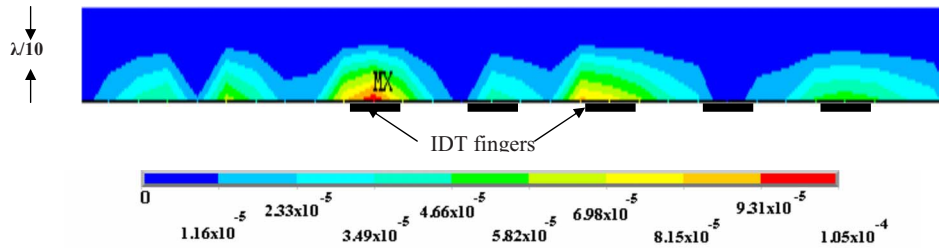

FIG. 8. (Color online) Shear stresses (MPa) generated as a result of the recirculation at the surface of the SAW device. The location of the IDTs is shown for visualization purposes. The applied input voltage was 0.1 V and the fluid viscosity was 10 cP. The magnitude of the induced shear stresses decreases with distance from the IDT fingers. Removal of nonspecifically bound proteins can be efficiently achieved if the induced shear forces are much larger than the binding constants of these proteins to the SAW device surface. A voltage value of 0.1 V is chosen for the purpose of illustration. Qualitatively similar behavior is observed at other applied voltages.

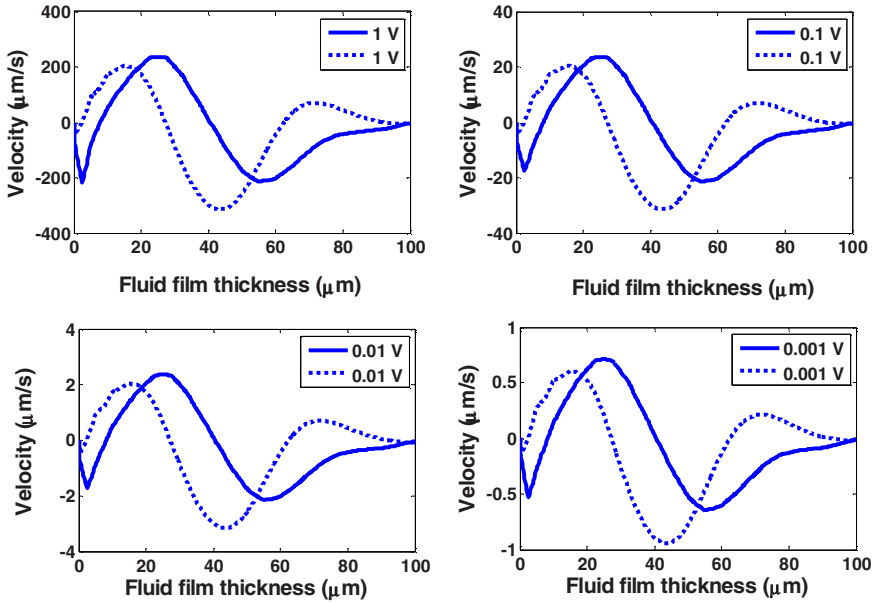

FIG. 9. (Color online) Simulated time-averaged tangential (solid lines) and normal (dashed lines) streaming velocity profiles along the thickness of the fluid film. The applied input voltage shown here varies from 1 mV to 1 V for a SAW device operating at 100 MHz. The streaming velocity profiles indicate reversal in flow direction and confirm the recirculation pattern observed in Fig. 7(b).

along the fluid film thickness normal to the piezoelectric substrate.

As seen in Fig. 9, most of the fluid motion is confined to within the first few layers (approxmately 70 μm). At distances >70 μm from the substrate surface, the wave motion is significantly dampened. This behavior is observed across the entire applied voltage range (0.001–100 V) simulated in this study. For any given applied voltage, we find that the extent of this wave damping is dictated by the shear viscosity of the fluid as well as the applied wave frequency. The streaming patterns near the device substrate are directly influenced by the motion of the piezoelectric substrate, whereas those further along the fluid film are induced by streaming flows from the lower surface. As a result, the liquid flow is attenuated in the process of inducing streaming motions near the top liquid surface (>80 μm). It can therefore be observed that the larger streaming velocities are observed at regions near the surface of the substrate (i.e., <40 μm).

The velocity profiles shown in Figs. 9 and 10 are indicative of reversal in flow direction at regions close to the SAW surface and at the center of the fluid region, thereby confirming the fluid circulation patterns shown in Fig. 7(b). At very short distances (<5 μm) close to the SAW surface, the tangential and normal velocity components attain a maximum before undergoing a flow reversal. In the region close to the fluid-solid interface, this corresponds to approximately 48 and 220 μm/s in the normal and tangential directions for an applied input voltage of 1 V. The first flow reversal for the tangential and normal components occurred at $\sim$2.5 and 0.2

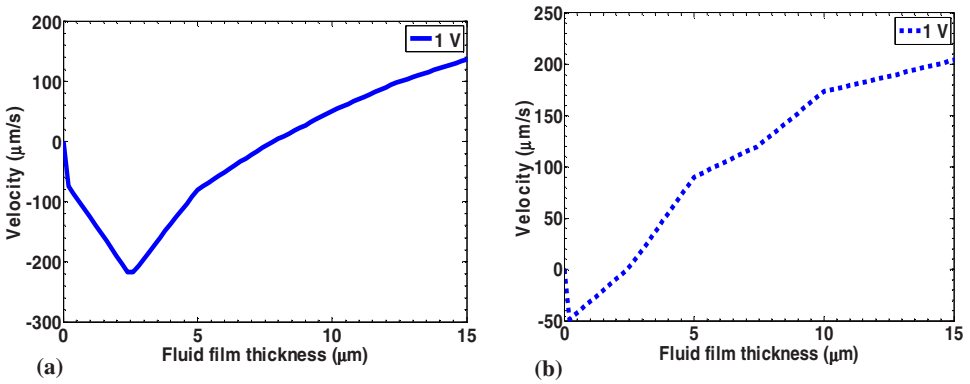

FIG. 10. (Color online) Simulated (a) tangential (solid lines) and (b) normal (dashed lines) streaming velocity profiles along the thickness of the fluid film at regions close to the surface of the piezoelectric substrate. The streaming velocity profiles indicate reversal in flow direction and confirm the recirculation pattern observed in our simulations. The applied input voltage for the streaming velocities shown here corresponds to 1 V. A voltage value of 1 V has been shown for the purpose of illustration. Qualitatively similar behavior is observed at other applied voltages.

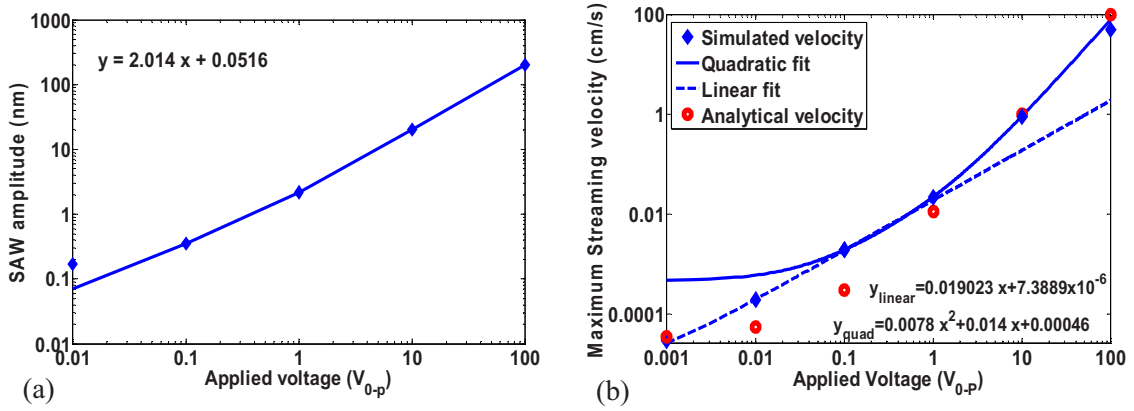

FIG. 11. (Color online) Variation of (a) SAW amplitude and (b) maximum streaming velocity with applied voltage. The amplitude of the SAW displacement varies linearly with applied input voltages for a SAW device operating at 100 MHz. The simulated maximum streaming velocity varies quadratically for applied input voltages greater than 0.1 V and linearly for lower applied voltages. Comparison with the analytical solution based on Nyborg's streaming theory is also shown in (b).

μm, respectively, as seen in the simulation data depicted in Figs. 10(a) and 10(b). At regions close to the fluid-solid interface (<5 μm), the tangential component of velocity has a larger magnitude than the normal for all the input voltages [Figs. 10(a) and 10(b)]. The maximum tangential flow velocity attained at regions close to the fluid-solid interface (<5 μm) before the first flow reversal varies approximately from 0.5 μm/s to 50 cm/s for the range of 0.001–100 V of input voltages as shown in Fig. 11(b). The predicted streaming patterns are in good agreement with the experimental observations of Guttenberg *et al.* [3].

The variation of SAW amplitude and the maximum streaming velocity with applied input voltage are shown in Figs. 11(a) and 11(b), respectively. The maximum streaming velocity is taken at regions close to the SAW surface, before the fluid undergoes the first reversal in flow direction. An increase in the applied input voltage results in a linear increase in the amplitude of SAW motion for applied voltages higher than 0.1 V, as shown in Fig. 11(a). As a result, the induced streaming velocities which typically vary as the square of the SAW displacement amplitudes [Eq. (3.16)] show a near quadratic behavior for input voltages higher than 0.1 V [6]. The simulated maximum streaming velocity shown in Fig. 11(b) agrees fairly well with the analytical solution formulated based on Nyborg's theory, at these higher applied voltages. At low voltages ($\leq$0.1 V), the analytical solution deviates slightly from the simulated streaming velocities, which could be attributed to the various approximations involved in deriving the streaming equations (Sec. III).

2. Effect of input excitation frequency

The effect of the excitation frequency on the acoustic-streaming velocity is presented in this section. The smallest attenuation in SAW devices is attained when the input excitation frequency matches the device frequency. The SAW device operational frequency is given by $v/4f$, where v is the velocity of the acoustic wave in YZ-$LiNbO_3$ and f is the IDT finger width. The above equation is valid only for a single split interdigital transducer configuration. Additionally, this equation is valid only for uniform spacing and finger widths. The IDT finger widths were modified to simulate SAW devices operating in different frequency ranges.

The streaming velocities represented in Fig. 12 correspond to SAW devices that operate at differing center frequencies, i.e., 100, 50, 10, and 1 MHz. The corresponding IDT finger width was 35, 70, 350, and 3500 μm, respectively. It should be noted that the scale of the simulated device was also increased in the same ratio, i.e., the substrate depth, propagation length, and liquid loading height were doubled when the finger spacing was changed from 35 to 70 μm. A similar procedure was adopted across the other two devices operating at 10 and 1 MHz frequency. Various input excitation frequencies with 1 V peak amplitude and matching the device frequency were applied. The streaming velocities along the fluid film thickness obtained at distance 2.5λ (where λ is the wavelength) along the delay path for input excitation frequencies of 100, 50, 10, and 1 MHz are shown in Fig. 12.

It is observed that the simulated streaming velocities increase with the device excitation frequency. We find that the tangential and normal components of the time-averaged streaming velocities near the SAW surface vary from approximately 220 and 48 μm/s, respectively, for a 100 MHz device to approximately 2.5 and 0.40 μm/s for a 1 MHz device with an applied peak voltage of 1 V. The simulated streaming velocities obtained in the μm/s range for devices operating in the MHz frequencies are in quantitative agreement with the experimental observations available in literature for streaming flows induced by SAW devices [2,30,43].

As the frequency of the surface-acoustic-wave device increases, it would lead to an increase in the irrotational velocity. This in turn results in an increase in the acoustic-streaming velocity which is proportional to the square of the irrotational velocity [1]. As shown in Eq. (3.8), the streaming velocity depends on the input excitation frequency as well as the leaky SAW wave number, which itself is a (linear) function of the SAW frequency. The tangential and normal veloc-

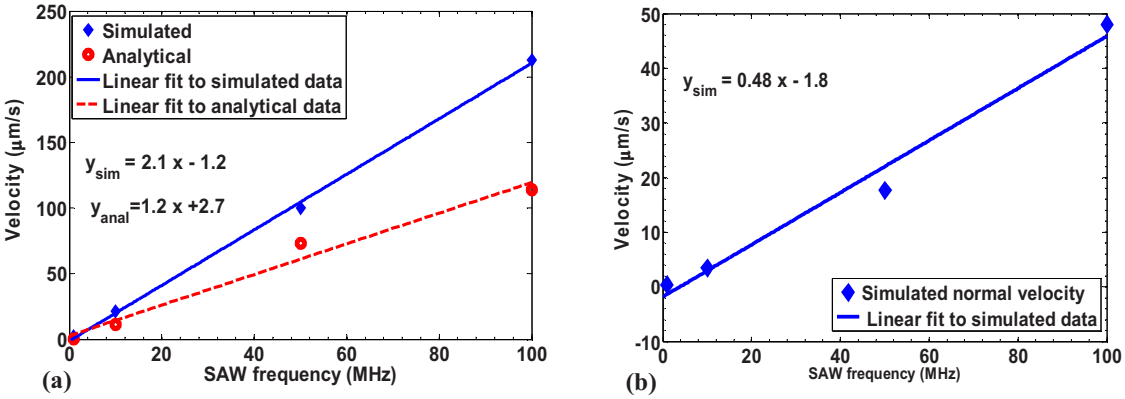

FIG. 12. (Color online) Effect of SAW device frequency on (a) tangential and (b) normal streaming velocities. The center frequency of the simulated SAW devices as well as the applied input voltage frequency was varied from 100 to 1 MHz. The simulated maximum streaming velocity varies linearly with the frequency of the SAW device. Comparison with the analytical solution based on Nyborg's streaming theory is also shown in (a).

ity profiles are therefore expected to vary as the square of the excitation frequency. However, the simulated streaming velocities in Fig. 12 show a near linear variation with the input excitation frequency. As brought out in Eq. (3.8), the acoustic-streaming velocity is also proportional to the square of the amplitude of SAW displacement. The simulated SAW amplitudes tend to increase with decreasing device frequency as shown in Table II. This has also been observed in the experimental studies of Sano *et al.* [2,52] Therefore, the increase in SAW amplitude somewhat offsets the corresponding decrease in the device frequency. As a result, the simulated and analytical SAW streaming velocities shown in Fig. 12 exhibit a near linear variation. It is interesting to note that the streaming velocities predicted analytically using Nyborg's theory are smaller than those from simulation. The analytical solution neglects the viscous effects and does not include attenuation of the flow, resulting in uniform streaming velocities across the fluid thickness.

The normal component of the velocity is significantly lower than the tangential for the range of device frequencies simulated in this work. This indicates that the surface normal component of the force exerted by the SAW is smaller than the tangential. Therefore, the lift-off forces would be smaller than the drag forces generated by acoustic streaming. This SAW streaming-induced drag force results in the advection of particles along the surfaces and appears to be an important step in the mechanism of particle removal using surface acoustic waves. The details of the various interaction forces involved and their influence on the particle removal mechanism is discussed in a subsequent section.

TABLE II. Variation of simulated SAW amplitudes for different device frequencies and input voltage of 1 V.

SAW device frequency (MHz)	SAW amplitude (nm)
100	2.15
50	3.45
10	6.84
1	10.53

3. Effect of fluid properties (viscosity and density)

To investigate the effect of fluid properties such as dynamic viscosity and density on the streaming velocity profiles, the FSI simulations were carried out under constant input conditions with only the fluid properties being varied. The effect of viscosity was investigated by simulating fluid loading with 1 and 10 cP viscosities, respectively. Among the various applied input voltages simulated in this study, the input voltage of 100 V represents conditions of maximum induced streaming velocities, and hence the effect of fluid viscosity is discussed at this applied input voltage. The results presented here represent the upper bound on the streaming velocity variations under varying fluid viscosities. For lower applied input voltages (<1 V), we find that the variation in the magnitude of the streaming velocities with fluid viscosity is not very significant at the MHz device frequencies.

The streaming velocities obtained for the two simulations at different locations along the SAW delay path are shown in Fig. 13. It can be seen that at the MHz frequencies, fluid viscosity variations have a significant effect on the streaming velocities, especially near the IDT region. As the wave propagates away from the input port along the $+Z$ propagation direction (henceforth termed the delay path to correspond to similar locations in an actual two-port SAW device), it undergoes significant attenuation as is evident from the reduction in the magnitude of the streaming velocity from approximately 50 to 15 cm/s near the fluid-solid interface for a propagation distance of approximately 2λ in a fluid having 1 cP viscosity. The effect of viscosity can be seen more prominently at distances further away from the IDT region when the wave has lost considerable energy. For locations further along the delay path (4λ), the streaming velocities rapidly decay to much smaller values (maximum of approximately 2 cm/s for 1 cP fluid along the fluid film thickness). The rapid decrease in the streaming velocities along the fluid film thickness is attributed to wave conversion into longitudinal modes (Sec. IV A). This decay length calculated from the instantaneous velocity at $t=60$ ns is approximately 40 μm at 10 μm delay and approximately 30 μm at 100 μm delay.

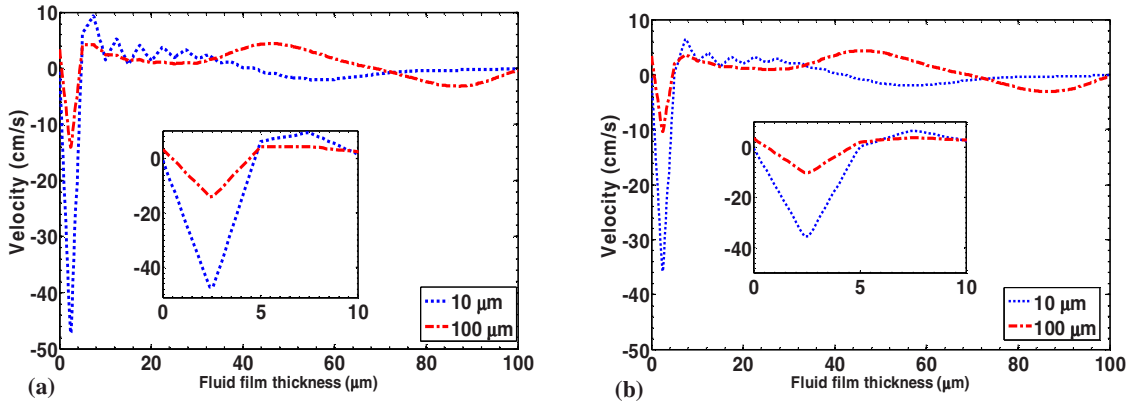

FIG. 13. (Color online) Streaming velocity profiles along the fluid film thickness for an applied input ac voltage of 100 V at 100 MHz and for two different fluid viscosities. (a) and (b) show streaming velocities calculated for two different fluid viscosities, i.e., 1 and 10 cP, respectively. The SAW device simulated in this work has one input or excitation port. 10 and 100 μm shown in (a) and (b) are distances from the outermost finger of the input port located along the $+Z$ propagation direction. The input voltage of 100 V represents conditions of maximum induced streaming velocities and hence the effect of fluid viscosity is shown at this applied input voltage.

Figure 14 demonstrates the relationship between the fluid viscosity and maximum streaming velocity as determined from our simulations. We find that an increase in the fluid viscosity leads to a decrease in the streaming velocities. The decrease in the streaming velocities is attributed to the increased viscous losses. The more viscous the fluid, the less would be the SAW-induced streaming force [10] for a given power input and hence the lower the extent of cleaning. This is in agreement with our experimental observations reported by Cular *et al.,* in which a reduced removal of nonspecifically bound proteins from the surface of a SAW biosensor device was reported for more viscous fluids [40].

The effect of density on the streaming phenomenon was evaluated by simulating fluids with properties similar to those of air (1 kg/m^3) and water (1000 kg/m^3). Although

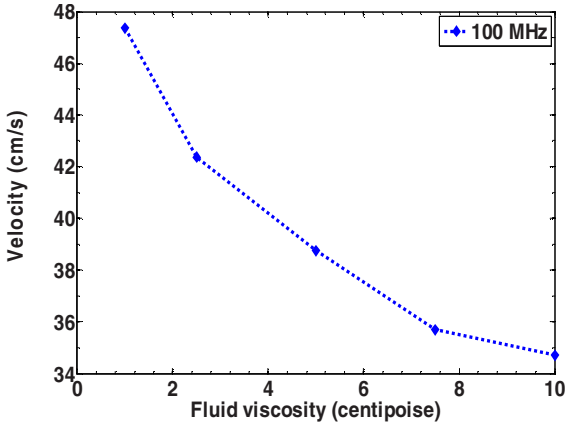

FIG. 14. (Color online) Variation in maximum streaming velocity for fluids of different viscosities. The applied input voltage was 100 V and the SAW device frequency was 100 MHz. The streaming velocities decrease with increase in fluid viscosity. The higher the fluid viscosity, the larger would be the force required to induce the SAW streaming and lower would be the efficiency of removal of nonspecifically bound proteins. The streaming velocities shown above are calculated at a distance of 10 μm from the outermost finger of the input port located along the $+Z$ propagation direction.

the viscosity of air (1.78×10^{-5} kg/m s) is significantly different from that of water (10^{-3} kg/m s), as brought out earlier, at MHz frequencies the viscous effects are not significant. Hence the differences in the streaming profiles would result mainly from the density difference between the two fluids. The simulation results for the two fluids for a SAW device operating at 100 MHz are shown in Fig. 15. The bulk compressibility factor (β) which is equal to the square of the sonic velocities was also varied in the simulations under study. The sonic velocities for air and water were taken as 340 and 1480 m/s, respectively. By specifying pressure $P=0$ at the top surface, an infinite reservoir of fluid was modeled.

The streaming velocity profiles as well as contours for the two fluids are shown in Figs. 15 and 16. It can be seen that significant qualitative and quantitative differences exist between the velocity profiles for the two fluids. The extent of wave attenuation in the case of air loading is much lower than that of water. Hence, the magnitude of streaming velocities obtained for air is an order of magnitude higher than for water loading. For lower-density fluids such as air, the velocities closer to the substrate are much lower than those in the center of the fluid region. As seen in Fig. 15(a), the maxima in SAW streaming velocity for both tangential (15 μm/s) and normal (8 μm/s) components occur at a distance of approximately 40 μm from the substrate. The increase in fluid density dampens the fluid motion. The magnitude of fluid motion close to the fluid interface is comparable to that away from the interface. These findings are in qualitative agreement with the experimental streaming velocity profiles, resulting from ultrasonic vibrations, obtained by Loh *et al.* using particle imaging velocimetry [53].

4. Forces involved in biofouling removal

As mentioned in Sec. II, SAW sensors used for detection of biological species suffer from fouling which results from binding of nonspecific protein molecules to the device surface. Fouling significantly lowers the sensitivity and selectivity as well as the sensor response speed. Removal of these

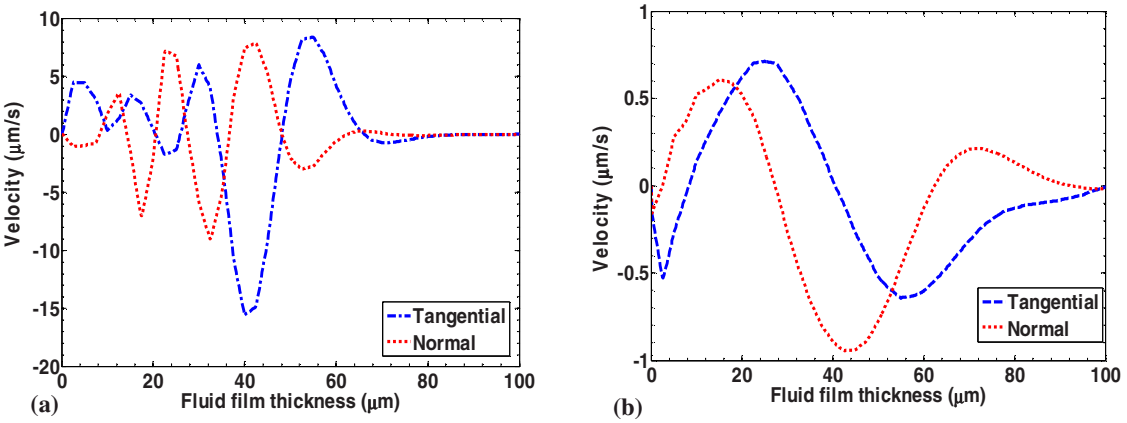

FIG. 15. (Color online) Simulated tangential and normal streaming velocity profiles along the fluid film thickness for an input ac voltage of 0.001 V in a SAW device operating at 100 MHz. The streaming velocities were calculated for two different fluid densities of (a) air and (b) water. It can be seen that even at very low applied input voltages such as 0.001 V, significant differences in the streaming velocity profiles and magnitudes exist for the two simulated fluid densities.

nonspecifically bound proteins would alleviate these problems and allow reuse of SAW devices. The finite-element analysis of SAW-induced acoustic-streaming phenomenon presented in this work indicates that the shear forces generated from the fluid motion can be high enough to ensure the removal of nonspecific proteins. The forces calculated analytically using the Campbell and Jones method [24,25] and Nyborg's theory [1] also corroborate this argument. Although an exact estimate of the principal adhesive forces such as van der Waals and electrical double layer involved in the binding of specific and nonspecific proteins to the SAW surface are required to identify the conditions which allow for higher removal efficiency, the streaming velocity fields and trends predicted in the current work can be utilized to understand the mechanism which is responsible for efficient removal of nonspecific proteins.

Typically, the cleaning forces on particles are hydrodynamic forces which could arise from linear as well as nonlinear interactions between the ultrasonic field and the particles in fluid [54]. Linear interaction forces include added mass, drag, lift, and Basset forces, whereas nonlinear ones include the drag forces that result from acoustic streaming. As mentioned in a previous section, the linear forces are time dependent and with mean value of zero whereas the

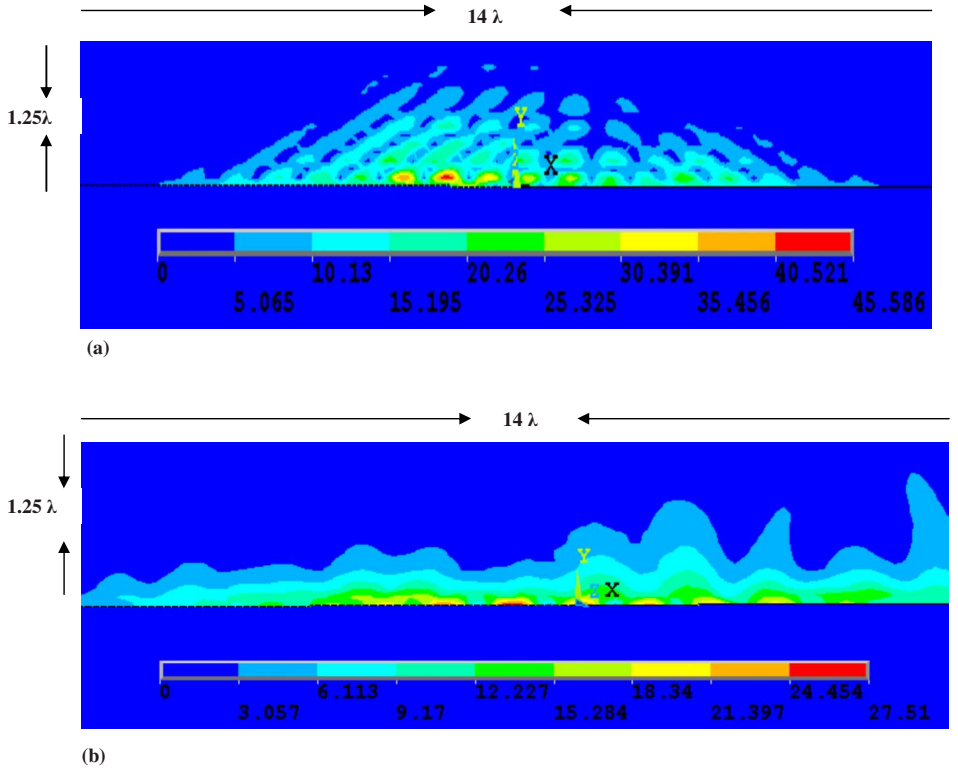

FIG. 16. (Color online) Contours showing the transient velocity field at $t=40$ ns for an input ac voltage of 0.001 V for a SAW device operating at 100 MHz and two different fluid densities of (a) air and (b) water. The velocities indicated by the scale bar are in μm/s. The displacements in the piezoelectric solid have been suppressed for clarity. The magnitudes as well as the streaming velocity patterns vary significantly in the two fluid media. It can be seen that the magnitude of induced streaming velocity is higher in the case of the less dense fluid. This indicates that higher removal efficiencies can be expected in case of less dense fluids. It can be seen that even at very low applied input voltages such as 0.001 V, significant differences in the velocity profiles exist for the two simulated fluid densities.

TABLE III. Forces (N) versus particle radius R (μm) for a 100 MHz SAW device and an applied input voltage of 10 V. The fluid viscosity is 1 cP. The calculated forces are based on the streaming velocity field generated at the IDT region. An applied voltage of 10 V is chosen simply for the purpose of illustrating the SAW removal mechanism.

	R		
	0.1	1	10
F_{vdW}	-2×10^{-9}	-2×10^{-8}	-2×10^{-7}
F_{SAW}	4×10^{-6}	4×10^{-4}	4×10^{-2}
F_L	2×10^{-16}	2×10^{-14}	2×10^{-12}
F_{ST}	1×10^{-12}	1×10^{-11}	2×10^{-10}

TABLE IV. Forces (N) versus particle radius R (μm) for a 100 MHz SAW device and an applied voltage of 10 V. The fluid viscosity is 1 cP. The calculated forces are based on streaming velocity field generated approximately 100 μm away from the IDT region. An applied voltage of 10 V is chosen simply for the purpose of illustrating the SAW removal mechanism.

	R		
	0.1	1	10
F_{vdW}	-2×10^{-9}	-2×10^{-8}	-2×10^{-7}
F_{SAW}	6×10^{-9}	6×10^{-7}	6×10^{-5}
F_L	1×10^{-19}	1×10^{-17}	1×10^{-15}
F_{ST}	1×10^{-13}	1×10^{-12}	2×10^{-11}

streaming-induced forces are time independent and, on averaging, have nonzero values. The magnitude of the linear interactions is larger than the nonlinear ones at moderate frequencies (kHz) whereas the nonlinear forces also assume significance at higher frequencies in the MHz range. The combined effect of the various interaction forces (adhesive and removal) is required to gain insights into the actual removal mechanisms. This, however, is beyond the scope of this study. Instead, useful insights into the dominant mechanism responsible for efficient removal of nonspecifically bound proteins can be obtained from the estimates of various forces predicted from the trends in the streaming velocity fields.

The dominant adhesive force for particle immersed in a liquid are the van der Waals and double-layer forces [55]. For the sake of simplicity, we assume that the nonspecifically bound proteins can be modeled as spherical particles of radius R. The van der Waals attraction force for a spherical particle near a flat surface is given by $F_{\mathrm{vdW}}\sim AR/6z^2$ where A is the Hamaker constant for the nonretarded force and z is the distance of maximum force of adhesion. Typical values of A in a liquid environment $\sim10^{-20}$ J. With increasing distance z, the van der Waals force becomes insignificant. Typical values of z are in the range of 0.2–0.4 nm. The van der Waals adhesion force for different particle radii is given in Table III. The electrical double-layer forces result from the electrostatic attraction and are associated with particle having effective diameters less than 5 μm. A surface contact potential created between two different materials based on the local energy state of each material results in the surface charge buildup. As a result, a double-layer charged region forms around the particle to preserve charge neutrality, leading to electrostatic attraction. For adhesion of submicrometer-sized particles, it was found that the electrical double-layer forces are of the same order of magnitude as the van der Waals forces and can be neglected in favor of the van der Waals force [56]. For the order of magnitude analyses of adhesion forces, it is usually sufficient to consider only the van der Waals force [54].

There are mainly three different mechanisms for particle removal, namely, sliding, rolling, and lift-off. The dominant mechanism can be established by comparing the relative magnitudes of the various removal forces. The forces responsible for removal of particles are mainly characterized as the direct SAW forces and the lift and the drag forces that result from the mean velocity field in the fluid. The direct SAW forces result from the wave propagation on the SAW-fluid interface and was discussed in detail in Sec. III A. The magnitude of the direct force is given by $F_{\mathrm{SAW}}\sim\sqrt{F_x^2+F_z^2}R^2$. The components of forces F_x and F_z are given by Eqs. (3.5) and (3.6). The fluid circulation around a particle results in inviscid lift forces, whose surface normal components act to remove the particle [57]. The lift forces can be estimated based on Bernoulli's equation by utilizing the pressure difference that exists between the bottom and top of the particle and is given by $F_L\sim\rho(u_xR)^2$. u_x and R refer to the surface normal component of velocity and the particle radius, respectively. The acoustic-streaming motion generated by SAWs leads to a drag force, caused by the interaction between the mean flow and the particles. The drag force which results from the boundary-layer-generated acoustic-streaming is given by $F_{\mathrm{ST}}\sim\mu Ru_z$. Here, u_z and μ refer to the tangential component of velocity and the fluid viscosity, respectively. Streaming is essentially parallel to the device surface and can potentially advect the particles along the surface. Thus, the relative magnitudes of the normal and tangential components of forces exerted by the SAWs on the fluid would dictate which of the three mechanisms is dominant. The SAW direct force as well as the lift and drag forces based on the velocity field generated in a 100 MHz SAW device for an applied input voltage of 10 V are given in Table III. The calculated forces are for particles that are located at the IDT region. The relative magnitude of the removal forces, i.e., lift, drag and the SAW direct forces, would change with increasing distance along the delay path. The increase in viscous dissipation results in rapid attenuation of streaming velocity with distance from the IDT region. The adhesive and removal forces calculated at approximately 100 μm away from the IDT region is shown in Table IV. The fluid density and viscosity were taken as 1000 kg/m^3 and 10^{-3} kg/m s, respectively. Based on the calculated adhesive and removal forces, a mechanism of removal of nonspecifically proteins can be predicted.

V. DISCUSSION

Experimental results for the removal of nonspecifically bound proteins using acoustic streaming induced by a SAW

device have been described in Sec. II A. These experimental observations demonstrate the concept of streaming-induced removal of nonspecifically bound proteins and confirm the findings of the FEM simulations that the SAW-induced acoustic-streaming phenomenon is an excellent method for surface stimulation in liquid environments. In this section, useful insights into the dominant mechanism responsible for efficient removal of nonspecifically bound proteins are sought from the estimates of various forces predicted on the basis of the FEM-generated streaming velocity fields.

Based on the order of magnitude analysis of the various forces listed in Table III, an approximate removal mechanism can be proposed. For micrometer- and submicrometer-sized protein agglomerates, the results in Table III illustrate that the fluid-induced removal forces are not significant enough to overcome the van der Waals forces at megahertz frequencies. F_{SAW} is several orders of magnitude greater than the adhesion forces for the range of particle diameters considered in Table III. It therefore appears that the SAW direct force causes the removal or detachment of the nonspecific proteins from the SAW surface and moves the particle away from the region of influence of the adhesive forces. As mentioned earlier, the van der Waals adhesion forces decrease rapidly with distance from the SAW surface. However, the SAW direct forces also decay rapidly with distance into the fluid. Hence, a steady force is required to cause the removal of the detached nonspecific proteins. The horizontal streaming-induced drag force (F_{ST}) helps to push the nonspecific proteins away from the fouled area. The vertical streaming force or the lift force (F_L) helps to prevent the readhesion of the proteins to the surface. Thus, the fluid-induced drag and lift forces result in a net displacement of the detached proteins.

Typically, the size of nonspecifically bound proteins is in the range of 50–100 nm. For a typical megahertz frequency device, the results in Tables III and IV illustrate the increasing difficulty in removing proteins (or agglomerates) of decreasing sizes. The submicrometer ($R<0.1$ μm) sized particles experience reduced removal forces and are much more difficult to remove. In accordance with the mechanism predicted above and the trends in the streaming velocity fields, it appears that the detachment of proteins would be higher for devices operating at higher frequencies and for higher applied input voltages. Also, the tangential as well as the normal streaming velocities increase for these operating conditions. Therefore, the drag and the lift forces generated would increase and facilitate removal of the detached proteins. With increasing fluid viscosity and density, we observe that the tangential and normal streaming velocities decrease. Hence, although the detachment of proteins might not be severely affected, the removal efficiency would decrease as a result of reduced drag and lift forces. Thus, removal of nonspecific proteins becomes increasingly difficult for fluids with higher viscosity and density. These observations are consistent with our experimental results reported by Cular *et al.* [40]

Based on the removal mechanism predicted and comparing the adhesive and removal forces in Tables III and IV, it can be seen that the removal efficiency, especially for submicrometer ($R=0.1$ μm) sized particles, decreases dramatically as we move away from the IDT region. A decay length can be defined which represents the region beyond which removal forces are not strong enough to eliminate biofouling. Based on the forces calculated in Tables III and IV, it can be said that the decay length for submicrometer-sized particles is approximately 100 μm for the above device. A similar analysis was also carried out for the SAW device operating at higher fluid viscosity of 10 cP. As brought out in the previous section, we find that at the MHz device frequencies simulated in the present work, the variation in streaming velocity for a fluid viscosity change from 1 to 10 cP is significant, especially at regions along the delay path located far away from the IDT region. We find that when the fluid viscosity is increased from 1 to 10 cP, the calculated decay length rapidly decreases from 100 to 60 μm. Therefore, our study indicates that, for increasing fluid viscosity in the range simulated in this work, the removal of nonspecifically bound proteins that can be efficiently carried out by SAW-induced streaming phenomenon decreases rapidly with increasing distance along the SAW delay path.

Although viscosity variations in simulations at ultrasonic frequencies (typically in the kHz range) have not been performed, experimental findings [9] indicate that at those frequencies the wave damping due to viscous dissipation would be higher. The viscous boundary layer involved is defined as $\delta=\sqrt{2}\nu/\omega$, where δ is the thickness of the viscous boundary layer, ν is the kinematic viscosity of the fluid medium, and $\omega=2\pi f$ is the angular frequency of the surface acoustic wave. For the range of viscosities employed in this study and the frequency of the surface waves, the thickness of the viscous boundary layer would be of the order of several micrometers at ultrasonic frequencies. For example, a SAW device operating at 100 kHz frequency and with a water loading ($\nu=1\times10^{-6}$ m^2/s), the thickness of the viscous boundary layer is 1.8 μm. Inside the boundary layer, there is eddy formation resulting from the circular flow as the medium has to confirm to the no-slip condition at the fluid-solid interface. The medium outside the boundary layer vibrates irrotationally in accordance with the sound field. Therefore, the extent of viscous dissipation resulting from the vortex formation near the SAW-fluid interface would be higher at ultrasonic frequencies than under megasonic frequencies and fluid viscosity would have a critical role to play.

It should be noted that the FSI model developed in this work employs only three IDT finger pairs. However, the experimental data (as shown in Fig. 1) typically have about 20–30 times this number of finger pairs. The acoustic power density is clearly different for the two cases. It is much higher in the case of the experimental study, which incorporates a larger number of finger pairs. In the case of the experimental study, we can observe that the removal of nonspecifically bound proteins is accomplished along the entire delay path, which is 197λ in length. This can be seen clearly from the data in Fig. 1. Based on the streaming velocities generated for the simulated SAW device with three finger pairs as well as the predicted mechanism of removal in the current finite-element study, we find that effective removal is accomplished only for a distance of approximately 3λ from the outermost IDT fingers. The differences clearly arise owing to the different acoustic power densities involved in the experimental and the simulated data. One possibility is to

normalize the streaming velocities with the number of IDT finger pairs. However, normalizing the velocity with finger pairs requires identification of the exact scaling factors involved. This would require fluid-solid interaction finite-element simulations of SAW devices with much larger number of finger pairs. The complex nature of the acoustic wave interaction with the fluid media as well as the limitations imposed by the computational requirements of such a model make it difficult to determine the exact scaling factors involved. Identification of these factors is beyond the scope the current study and requires a separate investigation of its own.

Furthermore, it is interesting to note that the FE-based results in the present work coincide well with the analytical solution calculated on the basis of Nyborg's streaming theory. In the case of Nyborg's theory, the only forces acting in shear are surface stresses due to the elasticity and viscosity. The bulk and shear viscosity are assumed to be constant. Nyborg's theory is based on the solution obtained by successive approximations applied to the Navier-Stokes equation. As brought out earlier, the first-order terms describe the oscillating part of the solution, which is related to the acoustic field, and whose time averages will be zero. Second-order terms are associated with time-independent components of the excess pressure, density, and velocity. These second-order components are associated with streaming. In the resulting Eqs. (3.1) and (3.2), terms higher than second order are assumed negligible and are discarded. This assumption limits the calculated streaming velocities to the low-Reynolds-number regime. Thus, the main drawback of the simpler analytical theory is the simplification of the Navier-Stokes equation to ignore higher-order terms which become important in the high-Reynolds-number regime.

For the range of input parameters studied in this work, the calculated streaming velocities were essentially found to be in the low-Reynolds-number regime and the flow is essentially laminar. This is the reason for the good agreement between the numerical FSI model and simple analytical theories. It should, however, be noted that at higher operational frequencies in the GHz range, the streaming velocities would be significantly higher and the induced flow might be in the turbulent regime. Under these conditions, the streaming velocities calculated using the FSI model are expected to be significantly different from those based on Nyborg's streaming theory. The increasing deviation between the analytical and FSI model with the SAW device operational frequency, in the streaming velocity plot shown in Fig. 11(a), corroborates this argument. Another major advantage of the current FSI model is that it can be extended to model non-Newtonian fluids as well. An analytical solution for such cases is clearly not possible.

VI. CONCLUSIONS

An analysis of acoustic streaming induced in a piezoelectric SAW device has been carried out. The flow induced by the Rayleigh wave generated on the SAW device surface with a liquid boundary layer was investigated. The SAW interaction with fluid leads to internal acoustically induced streaming and results in mode conversion to a longitudinal leaky SAW, which decays exponentially with distance in the fluid. The velocity vector field shows recirculation patterns in the fluid region resulting from the out-of-phase motion of the IDT fingers. The fluid recirculation exerts steady viscous stresses on the interphase boundaries which can be used for the removal of nonspecifically bound proteins. The extent of recirculation and therefore the induced stresses were found to decrease with distance from the IDT fingers.

Optimization of parameters that can maximize the streaming and cause removal of unwanted proteins along the entire delay path is required. Toward this end, the effects of several design parameters such as input voltage amplitude and frequency as well as fluid properties such as density and viscosity were studied. It was found that the variation in induced streaming velocity was nearly linear for low amplitude of the applied voltage and quadratic with a higher input voltage. Therefore, the higher the applied voltage the greater will be the extent of acoustically induced streaming. For devices operating at higher frequency, the simulations predict increased streaming velocities. In all cases, the tangential component of streaming velocity was higher than the normal component. The effect of fluid properties such as viscosity and density on the SAW-induced streaming was also investigated. The simulations predict a decrease in streaming velocity with increasing fluid viscosity and density. Therefore, for more viscous and dense fluids, the extent of streaming induced by SAWs under a given operating condition would be lower. The model predictions are in fairly good agreement with the analytical solution formulated on the basis of Nyborg's theory and the Campbell-Jones method.

The predicted streaming velocity fields as well as the trends in their variation for a range of operating conditions were utilized to compute the various forces generated in a typical SAW cleaning operation. An order of magnitude comparison of the various forces involved in the SAW cleaning operation was further used to predict the mechanism involved in the removal of nonspecifically bound proteins. It appears that the removal of these proteins can be viewed as a combined process which involves overcoming adhesion forces, lifting them from the SAW surface, and convecting them away. Based on the predicted cleaning mechanism and the velocity fields computed using the finite-element model, we find that the removal efficiency is higher for devices operating at higher frequencies and for higher applied input voltages. Also, particles that are smaller in size are difficult to remove. The increase in fluid viscosity and density reduces the efficiency of removal of nonspecifically bound proteins for a device operating at a given frequency and applied input voltage. This agrees well with the experimental observations. It is expected that the model-generated trends in conjunction with the proposed mechanism would serve as guidelines for subsequent experimental investigations.

ACKNOWLEDGMENTS

The authors wish to thank the Academic Computing Center and the Engineering Computing Center at University of South Florida for providing the computational facilities. We

gratefully acknowledge financial support provided by the NSF Grant No. DGE 0221681, the Department of Defense Contract No. W81XWH-05-1-0585, and the USF Office of Research through an interdisciplinary research grant. The authors thank Dr. Richard Lange and Dr. Bill Bullat at ANSYS Inc. and Reetu Singh of USF for useful discussions.

[1] W. Nyborg, *Acoustic Streaming* (Academic, New York, 1965).
[2] S. Shiokawa, Y. Matsui, and T. Moriizumi, Jpn. J. Appl. Phys., Part 1 **28**, 126 (1989).
[3] Z. Guttenberg, A. Rathgeber, S. Keller, J. O. Raedler, A. Wixforth, M. Kostur, M. Schindler, and P. Talkner, Phys. Rev. E **70**, 056311 (2004).
[4] R. M. Moroney, R. M. White, and R. T. Howe, Appl. Phys. Lett. **59**, 774 (1991).
[5] N. T. Nguyen and R. M. White, Sens. Actuators, A **77**, 229 (1999).
[6] N. T. Nguyen and R. M. White, IEEE Trans. Ultrason. Ferroelectr. Freq. Control **47**, 1463 (2000).
[7] G. G. Yaralioglu, I. O. Wygant, T. C. Marentis, and B. T. Khuri-Yakub, Anal. Chem. **76**, 3694 (2004).
[8] R. H. Nilson and S. K. Griffiths, J. Electrochem. Soc. **149**, G286 (2002).
[9] K. Bakhtari, R. O. Guldiken, P. Makaram, A. A. Busnaina, and J.-G. Park, J. Electrochem. Soc. **153**, G846 (2006).
[10] K. R. Nightingale and G. E. Trahey, IEEE Trans. Ultrason. Ferroelectr. Freq. Control **47**, 201 (2000).
[11] J. Kondoh, N. Shimizu, Y. Matsui, and S. Shiokawa, IEEE Trans. Ultrason. Ferroelectr. Freq. Control **52**, 1881 (2005).
[12] M. Kurosawa, T. Watanabe, A. Futami, and T. Higuchi, Sens. Actuators, A **50**, 69 (1995).
[13] K. Miyamoto, S. Nagatomo, Y. Matsui, and S. Shiokawa, Jpn. J. Appl. Phys., Part 1 **41**, 3465 (2002).
[14] C. M. Gregory, J. V. Hatfield, S. Higgins, H. Iacovides, and P. J. Vadgama, Sens. Actuators, B **65**, 305 (2000).
[15] N. Wisniewski and M. Reichert, Colloids Surf., B **18**, 197 (2000).
[16] S. Sharma, R. W. Johnson, and T. A. Desai, Biosens. Bioelectron. **20**, 227 (2004).
[17] S. Cular, V. R. Bhethanabotla, and D. W. Branch, Proc.-IEEE Ultrason. Symp. **4**, 2309(1995).
[18] L. A. Kuznetsova and W. T. Coakley, Biosens. Bioelectron. **22**, 1567 (2007).
[19] J. D. Ballantine, R. White, S. Martin, A. Ricco, E. Zellers, G. Frye, H. Wohltjen, M. Levy, and R. Stern, *Acoustic Wave Sensors, Theory, Design, & Physico-Chemical Applications* (Academic, Boston, MA, 1997).
[20] F. Josse, F. Bender, and R. W. Cernosek, Anal. Chem. **73**, 5937 (2001).
[21] Z. Li, Y. Jones, J. Hossenlopp, R. W. Cernosek, and F. Josse, Anal. Chem. **77**, 4595 (2005).
[22] J. Kondoh and S. Shiokawa, Proc.-IEEE Ultrason. Symp. **2**, 716 (1995).
[23] S. Shiokawa, Y. Matsui, and T. Ueda, Proc.-IEEE Ultrason. Symp. **1**, 643 (1989).
[24] J. J. Campbell and W. R. Jones, IEEE Trans. Sonics Ultrason. **15**, 209 (1968).
[25] J. J. Campbell and W. R. Jones, IEEE Trans. Sonics Ultrason. **17**, 71 (1970).
[26] L. G. Olson, J. Sound Vibr. **126**, 387 (1988).
[27] T. Xue, W. Lord, and S. Udpa, IEEE Trans. Ultrason. Ferroelectr. Freq. Control **44**, 557 (1997).
[28] K. Chono, N. Shimizu, Y. Matsui, J. Kondoh, and S. Shiokawa, Proc.-IEEE Ultrason. Symp. **2**, 1786 (2003).
[29] K. Chono, N. Shimuzu, Y. Matsui, J. Kondoh, and S. Shiokawa, Jpn. J. Appl. Phys., Part 1 **43**, 2987 (2004).
[30] T. Uchida, T. Suzuki, and S. Shiokawa, Proc.-IEEE Ultrason. Symp. **2**, 1081 (1995).
[31] S. Furukawat, T. Nomuraz, and T. Yasudaz, J. Phys. D **24**, 706713 (1991).
[32] B. D. Ratner, F. J. Hoffmann, J. E. Schoen, and F. Lemons, *Biomaterials Science: An Introduction to Materials in Medicine* (Academic, San Diego, CA, 1996).
[33] S. Sharma, R. W. Johnson, and T. A. Desai, Biosens. Bioelectron. **20**, 227 (2004).
[34] N. Wisniewski and M. Reichert, Colloids Surf., B **18**, 197 (2000).
[35] A. Halperin, Langmuir **15**, 2525 (1999).
[36] R. G. Chapman, E. Ostuni, S. Takayama, R. E. Holmlin, L. Yan, and G. M. Whitesides, J. Am. Chem. Soc. **122**, 8303 (2000).
[37] R. Hamburger, E. Azaz, and M. Donbrow, Pharm. Acta Helv. **50**, 10 (1975).
[38] R. S. Kane, P. Deschatelets, and G. M. Whitesides, Langmuir **19**, 2388 (2003).
[39] V. A. Tegoulia, W. Rao, A. T. Kalambur, J. F. Rabolt, and S. L. Cooper, Langmuir **17**, 4396 (2001).
[40] S. Cular, D. W. Branch, G. D. Meyer, and V. R. Bhethanabotla, in *AIChE Annual Meeting, Conference Proceedings, Cincinnati, OH* (Omnipress, Atlanta, GA, 2005), p. 526c/1.
[41] M. K. Aktas and B. Farouka, J. Acoust. Soc. Am. **116**, 2822 (2004).
[42] A. K.-H. Chu, Phys. Rev. E **72**, 066311 (2005).
[43] R. M. Moroney, Ph.D. thesis, University of California, Berkeley, 1995 (unpublished).
[44] R. M. Moroney, R. M. White, and R. T. Howe, Proc.-IEEE Ultrason. Symp. **1**, 355 (1990).
[45] M. S. Longuet-Higgins, Philos. Trans. R. Soc. London, Ser. A **245**, 535 (1953).
[46] Computer code ANSYS, v. 10 (ANSYS Inc., www.ansys.com). ANSYS is a general purpose finite-element modeling package for numerically solving a wide variety of mechanical problems. The ANSYS multiphysics software, which is a comprehensive coupled physics tool combining structural, thermal, computational fluid dynamics, acoustic, and electromagnetic simulation capabilities, was employed in this current work.
[47] B. A. Auld, *Acoustic Fields and Waves in Solids* (Wiley, New York, 1973).
[48] T. J. R. Hughes, W. K. Liu, and T. K. Zimmermann, Comput. Methods Appl. Mech. Eng. **29**, 329 (1981).
[49] J. Donea, S. Giuliani, and J. P. Halleux, Comput. Methods

Appl. Mech. Eng. **33**, 689 (1982).
[50] T. J. R. Hughes, *The Finite Element Method Linear Static and Dynamic Finite Element Analysis* (Prentice-Hall, Englewood Cliffs, NJ, 1987).
[51] S. K. R. S. Sankaranarayanan, V. R. Bhethanabotla, and B. Joseph, ECS Trans. **1**, 19 (2006).
[52] A. Sano, Y. Matsui, and S. Shiokawa, Proc.-IEEE Ultrason. Symp. **1**, 467 (1997).
[53] B.-G. Loh, D.-R. Lee, and K. Kwon, Appl. Phys. Lett. **89**, 183505 (2006).
[54] Q. Qi and G. J. Brereton, IEEE Trans. Ultrason. Ferroelectr. Freq. Control **42**, 619 (1995).
[55] J. Israelachvili, *Intermolecular and Surface Forces* (Academic, London, 1992).
[56] H. Krupp, *Particle Adhesion Theory and Experiment* (Elsevier, New York, 1967).
[57] D. A. Drew, Chem. Eng. Sci. **43**, 769 (1988).